

1 Spatiotemporal Variability and Environmental Controls on Aquatic Methane Emissions in an Arctic
2 Permafrost Catchment

3 Michael W. Thayne¹, Karl Kemper^{1,2}, Christian Wille¹, Aram Kalhori¹, & Torsten Sachs^{1,3}

4 ¹ GFZ Helmholtz Centre for Geosciences, Potsdam, Germany

5 ² Department of Geosciences, University of Cologne, Cologne, Germany

6 ³ Institute of Geoecology, Technical University of Braunschweig, Braunschweig, Germany

7 Correspondence email: Michael W. Thayne (m_thayne@me.com)

8 Abstract

9 Understanding spatiotemporal dynamics and drivers of methane (CH_4) fluxes from rapidly changing
10 permafrost regions is critical for improving our understanding of such changes. Between May and
11 August 2023 and 2024, we measured CH_4 using floating chambers in a small Arctic permafrost
12 catchment on Disko Island, Greenland. Fluxes were derived from 707 chamber measurements using
13 a semi-automated algorithm incorporating boosted regression trees and generalized additive
14 models. Highest fluxes occurred in streams and along lakeshores associated with inlets. Diffusive
15 fluxes dominated (~98% of observations), while only ~1% of chamber deployments exhibited non-
16 linear concentration increases indicative of ebullition, while the other ~1% were attributed to
17 uptake. Median diffusive fluxes were $5.0 \text{ nmol m}^{-2}\text{s}^{-1}$, (-0.1 to 271.8), peaking at ice-break. Ebullition
18 had a median of $939 \text{ nmol m}^{-2}\text{s}^{-1}$ (5.2 - 14,893), but did not impact overall fluxes. Model results
19 suggest that thaw-season CH_4 fluxes were initially driven by meteorological conditions and
20 catchment soil conditions, but shifted rapidly—within approximately one week after ice-off—to
21 biogeochemical controls, including dissolved organic matter, oxygen saturation, and pH.

22 1 Introduction

23 Permafrost regions across the Arctic store substantial amounts of carbon. Climate warming
24 is rapidly changing permafrost regions and consequently their carbon storage dynamics, creating a
25 critical climate feedback mechanism (Schuur et al., 2015; Miner et al., 2022). At current warming
26 rates, models project approximately 77% of shallow permafrost will be lost by 2100 (Fox-Kemper et
27 al. 2021), suggesting large implications for the global carbon budget and how carbon emissions are
28 distributed across permafrost landscapes. The underlying issue is that thawing permafrost can
29 release previously frozen organic matter, delivering labile nutrients to soil microbes which accelerate
30 the decomposition of soil organic carbon as a result of their metabolic processes (Schuur et al., 2015;
31 Keskitalo et al., 2021; Olefeldt et al., 2021). Subtle changes in microbial processes in soils can
32 enhance positive feedback mechanisms which compounds atmospheric warming. Lateral movement
33 of water through active layer soils is a critical pathway for CH_4 emissions from surface waters (Street
34 et al., 2016; Olid et al., 2021, 2022; Fazi et al., 2021). Hydrological and catchment system dynamics in
35 particular play a critical role in distributing dissolved carbon throughout permafrost environments.
36 Catchment systems, such as thermokarst lakes and wetlands, have been shown to be “hotspots” for
37 CH_4 release, where daily emission rates between 10 and $200 \text{ mg m}^{-2}\text{d}^{-1}$ have been reported (Walter
38 Anthony et al., 2018; Elder et al., 2020). However, while localized high emissions have been
39 reported, the overall contribution of Arctic and permafrost freshwater bodies to global methane
40 budgets is fairly low at 2-6% when compared to other ecoregions such as the tropics at 64%
41 (Bastviken et al., 2004; Saunois et al., 2025; Virkkala et al., 2024). Nonetheless, with such drastic
42 change expected, well designed field studies exploring which processes are the most important for

43 governing CH₄ emissions from permafrost regions, are critical data sources for validating climate
44 models and simulations (Bartsch et al. 2025).

45 Carbon dynamics in permafrost regions have been shown to be governed by interactions
46 between soil, vegetation, hydrology, and atmospheric processes (Walter Anthony et al., 2012;
47 Virkkala et al., 2024; Yuan et al., 2024; Kleber et al. 2025). Located on the central-west coast of
48 Greenland, Qeqertarsuaq, also known as Disko Island, has become an important data point for
49 understanding environmental interactions which govern Arctic tundra carbon dynamics. The island
50 provides a natural laboratory for observing interactions between permafrost, vegetation, microbial
51 activity and aquatic ecosystems (Humlum, 1998; Humlum et al., 1999; Callaghan et al., 2011;
52 Christiansen et al., 2015; D'Imperio et al., 2017). Previous work from the study area has suggested
53 shifting hydrology, historic permafrost thaw, nutrient cycling, and microbial activity in the active and
54 permafrost layers as possible drivers of CH₄ fluxes from surface water bodies (Zastruzny et al., 2017;
55 Kluge et al., 2021; Stevenson et al., 2021; Juncher Jørgensen et al., 2024). These studies highlight the
56 interconnectedness of terrestrial and aquatic ecosystems, and the effect they may have on CH₄
57 fluxes from lakes and streams on Disko Island. There is yet to be an extensive study on CH₄ fluxes
58 from the island's lakes and streams. However, it has been suggested that permafrost thaw and
59 warming air temperatures may have an effect on greenhouse gas fluxes (Kluge et al., 2021; Juncher
60 Jørgensen et al., 2024). Soil warming experiments and studies of increased snow cover in winter
61 were shown to regulate carbon fluxes through accelerated carbon turnover (Ravn et al., 2020; Xu et
62 al., 2021). Carbon fluxes are further controlled by plant uptake and through microbial activity
63 regulating the availability of nutrients and subsequent CH₄ production (Laanbroek, 2010; Liebner et
64 al., 2011; D'Imperio et al., 2017). Sedimentary processes in lakes promote carbon storage, whereas
65 methanotrophic and methanogenic microbial assemblages along an upland–wetland environmental
66 gradient regulate CH₄ consumption and emission, respectively. Therefore, freshwater ecosystems
67 play a critical role storing, producing, and emitting CH₄ (Christiansen et al., 2015; Žárský et al., 2018;
68 Stevenson et al., 2021).

69 The hydrology of Disko Island is strongly influenced by past volcanic activity during the
70 Paleocene epoch. With extensive basaltic lava flows characterizing the landscape, the island's terrain
71 is formed by the Maligåt and Vaigat Formations, which are comprised of highly permeable layers of
72 basalt interbedded with fluvial and lacustrine sediments (Westergaard-Nielsen et al., 2020; Larsen &
73 Larsen, 2022). The high permeability of these geologic formations enables substantial subsurface
74 flow, subsequently forming perennial water features such as warm springs. In spring, the soils which
75 make up the active layer allow for rapid infiltration of meltwater, which laterally distributes
76 nutrients and organic matter throughout the island's aquatic ecosystems (Westergaard-Nielsen et
77 al., 2020). For example, during spring runoff meltwater and hillside topography was found to largely
78 drive the distribution of nitrates from terrestrial to aquatic ecosystems (Zastruzny et al., 2017;
79 Stevenson et al., 2021). Thus, pools of nutrients available during the growing season may vary
80 dramatically from one year to the next. Lateral flow of snowmelt and permafrost thaw may influence
81 CH₄ fluxes due to changes in physio- and biogeochemical properties of the lakes, streams and rivers
82 on the island (Liebner et al., 2011; Rautio et al., 2011; Walvoord & Kurylyk, 2016; Stevenson et al.,
83 2021). Although Disko Island has discontinuous permafrost (Christiansen et al., 2015; Kluge et al.,
84 2021), thawing can release trapped organic matter and nutrients into aquatic ecosystems,
85 potentially affecting CH₄ fluxes by providing new substrates for microbial activity (Ravn et al., 2020;
86 Stevenson et al., 2021; Westergaard-Nielsen et al., 2020; Xu et al., 2021).

87 The distribution and drivers of aquatic CH₄ emissions in permafrost regions remain poorly
88 constrained, particularly across small lakes and streams which may arise as emission hotspots.

89 Previous studies on Disko Island have highlighted the potential importance of hydrology, permafrost
90 thaw, and microbial processes for greenhouse gas fluxes, but comprehensive spatial and seasonal
91 assessments of CH₄ are lacking. In this study we address this gap by quantifying CH₄ fluxes from 707
92 floating chamber measurements across a permafrost-affected catchment (Sanningasup Tasia). Using
93 boosted regression trees, we evaluate the partial effects of physiochemical water conditions,
94 catchment soil conditions, and meteorology in regulating emissions from ice-break through the
95 growing season. Our objective was to determine how spatial heterogeneity and seasonal dynamics
96 shape CH₄ emissions from Arctic freshwater ecosystems and to identify the key processes that
97 control flux variability in permafrost catchments.

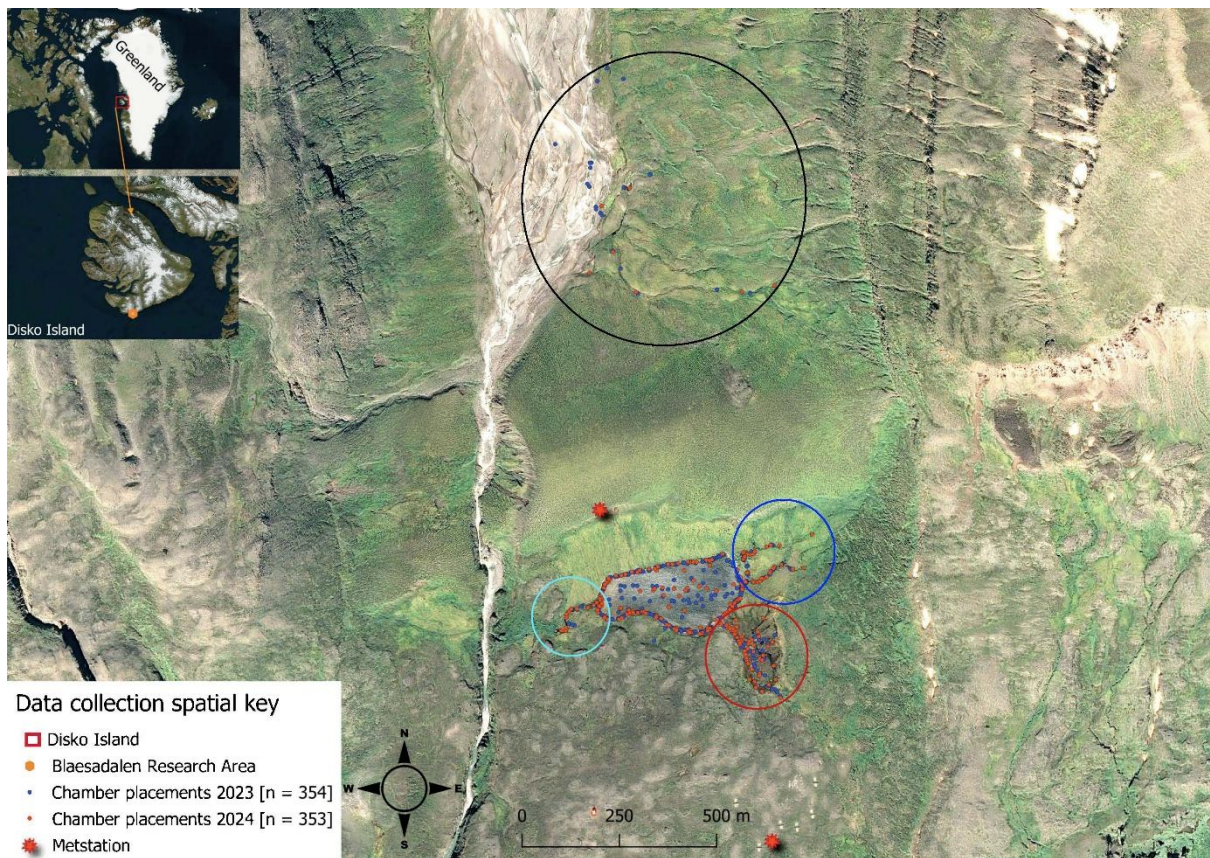
98 2 Methods

99 2.1 Study Site

100 Lake Sanningasup Tasia in Greenlandic, or Moræne sø in Danish, is situated between
101 moraines in the north and east and an outlet which drains into the Red River to the west (Figure 1).
102 The lake is primarily fed by a large warm spring which enters the lake from the southeast, forming a
103 wetland type ecosystem. The other inlets of the lake are primarily fed by seasonal snowmelt. The
104 heterogeneity of the catchment provides an exemplary study site, allowing us to understand the
105 mechanisms regulating CH₄ emissions from a lake, streams, and wetland. According to a 2018 report
106 from the University of Copenhagen, the lake has a maximum depth of 4.5 m and is generally
107 phosphorus limited with nitrogen concentrations being seasonally variable, where concentrations
108 during ice cover are higher than during periods of no ice cover (Westergaard-Nielsen et al., 2020).
109 We found water temperature of the lake to range between 1.1 and 13.9 °C with a mean of 7.9 °C. To
110 our knowledge there has never been an extensive study on the greenhouse gas fluxes from the lake
111 and surrounding water bodies.

112

113



122

Figure 1. Map showing the 707 chamber measurements (blue and brown dots). Points in the south are concentrated around Lake Sanningasup Tasia and its connected streams. The blue circle indicates streams fed by snowmelt and the turquoise circle indicates the outlet of the lake. The red circle indicates the warm spring area which forms a wetland type ecosystem. Points inside the black circle north of the lake indicate measurements taken from the Red River and its stream tributaries.

123

124

125

126

127

128

129

130

131

132

133

134

135

136

137

2.2 Data Collection

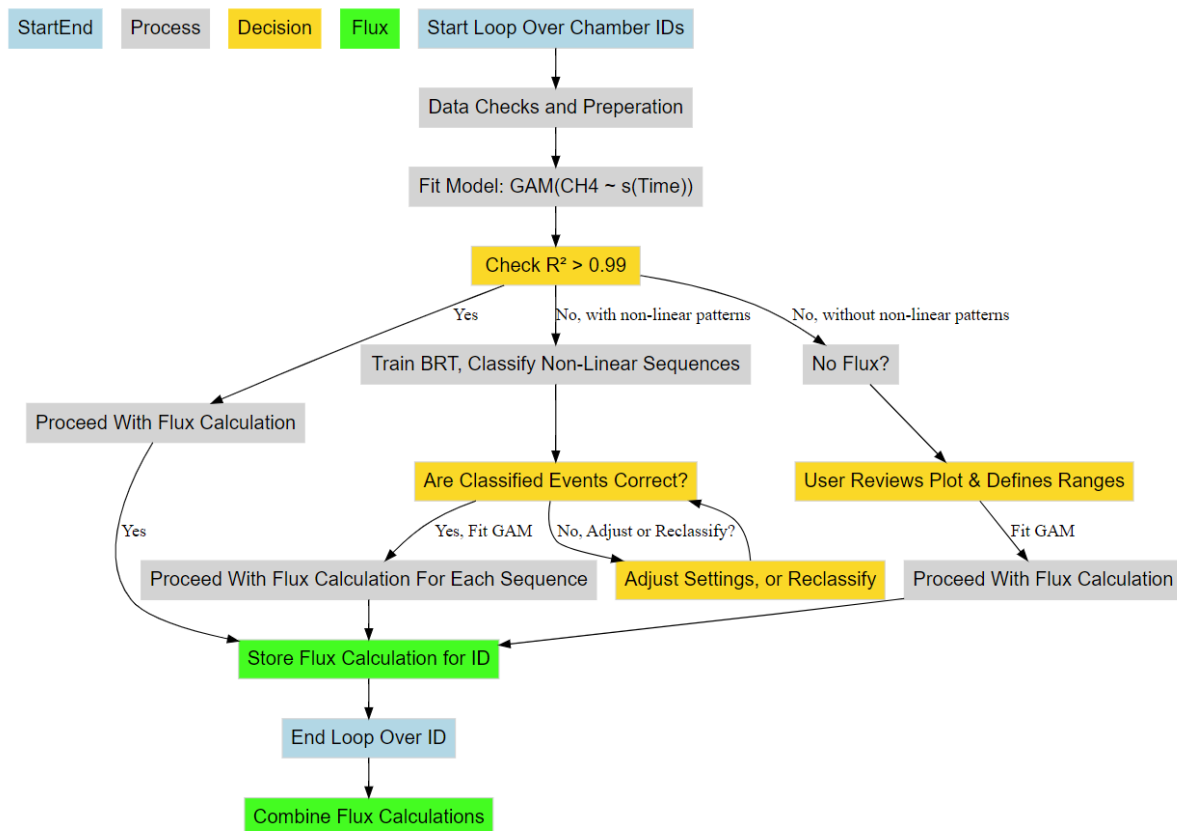
We used closed floating chamber systems connected to an ABB/Los Gatos Research GLA131 Series Micro portable Gas Analyzer in 2023, and to a LI-COR® LI-7810 Trace Gas Analyzer in 2024, with the goal of capturing the spatial and temporal variability of CH₄ fluxes in the catchment area. In 2023, we used a self-built cylindrical chamber made of semi-transparent plastic material with volumetric capacity of 0.016 m³ and a basal area of 0.096 m². In 2024, we used a West Systems type C flux chamber made of stainless steel with a volumetric capacity of 0.013 m³ and a basal area of 0.07 m². Both chambers included a fan for mixing air and a temperature sensor. The semi-transparent plastic chamber used a circular foam floater that was wrapped around the outside of the chamber, allowing 2cm of the chamber to be below the water surface, forming a 100% airtight seal. The West Systems chamber was inserted into a closed-cell foam floater, where the seal was created once the chamber was inserted into the floater. Despite differing chamber materials and flotation devices, median fluxes between 2023 and 2024 were identical at 5.0 nmol m⁻²s⁻¹. However, to evaluate whether changes in chamber construction between years introduced systematic bias in CH₄ flux estimates, we fit a linear model using log-transformed flux as the response and chamber type, latitude, longitude, and Julian day as predictors. Chamber type was not a significant predictor

138 ($p = 0.13$), and QQ plots of log-transformed fluxes across years showed no consistent deviation
139 across the flux distribution, except at lower emission rates (Figure S1). These findings suggest that
140 differences in chamber construction did not substantively influence the calculated fluxes. Chamber
141 measurements were conducted on the surface of the lake and surrounding water bodies at a spatial
142 distance of 10 to 20 m with a closure time of 10 minutes. The chamber and gas analyzer were
143 connected in a closed loop, and sample air was continuously pumped through the gas analyzer. CH₄
144 concentrations were measured with a frequency of 1 Hz. Each flux measurement was given a unique
145 id based on its spatial location or water body type. For the lake, ids were given based on what
146 shoreline we were measuring on. For example, if on the east shore, ids would be e1, e2, e3, ... etc.
147 The majority of flux measurements on the lake were conducted within 0.2 m from the shore. Open
148 water measurements in the lake were made using a small boat and anchor system. CH₄
149 concentrations in streams were measured by starting at, or near the headwaters and then taking
150 measurements progressively downstream with consideration to the changing terrestrial vegetation
151 and stream dynamics (i.e., fast, slow, or eddie pool). In 2023, we measured isolated meltwater pools
152 during the thaw to represent control conditions (water not yet connected to the lake or streams). In
153 2024, to capture an even earlier baseline, we conducted chamber measurements on top of snow
154 and lake ice prior to thaw onset, providing a true pre-thaw control period. Overall, we made 707
155 chamber measurements, representing ~10-15 chamber placements taking place daily, around the
156 lake and surrounding streams giving us an extensive view of the spatial and temporal variability of
157 CH₄ fluxes in the study area. While floating chambers isolate the headspace from light wind
158 disturbance, increased surface turbulence may influence gas exchange in the open space of the
159 chamber (Vachon and Prairie 2013). Our approach captures diffusive exchange under mostly
160 calm-water conditions (i.e., wind speed up to ~4 ms⁻¹), but we acknowledge that regional wind-
161 driven mixing may contribute to flux variability beyond individual chamber footprints. We
162 simultaneously measured water temperature using Truebner EC-100 RS-485 EC/Temperature
163 sensors in 2023 and a suite of water parameters were collected in 2024 using an AquaTroll 600
164 water sonde (see section: Decoding Methane Drivers). Meteorological data and soil characteristics
165 were collected from nearby meteorological stations maintained by Aarhus University which are part
166 of the Greenland Ecosystem Monitoring Database (Greenland Ecosystem Monitoring, 2025a-d) (see
167 section “Decoding Methane Drivers” for list of variables used).

168 2.3 Flux Algorithm & Ebullition Detection

169 In collaboration with ChatGPT 4.0, we wrote an interactive algorithm in R which leverages
170 General Additive Models (GAM) and Boosted Regression Trees (BRT) to robustly and flexibly
171 calculate CH₄ fluxes from individual floating chamber measurements (Figure 6). The flux calculation
172 procedure was applied identically to individual chamber time series for both 2023 and 2024, while
173 controlling for different the chamber constructions.

174



175

176 Figure 2. CH₄ flux calculation workflow from concentration data using predictions from GAM and
 177 BRT. Blue boxes represent the start and end of a single chamber measurement working through the
 178 algorithms processes (grey boxes) and decision logic (gold boxes). Green boxes represent the storage
 179 and combination of the results for further analysis.

180 Rather than fitting concentration data with linear, exponential, and/or polynomial models
 181 (Kutzbach et al., 2007; Pedersen et al., 2010; Hoffmann et al., 2017), the algorithm fits GAM, which
 182 are capable of modelling non-linear patterns without a-priori specification of the functional form of
 183 the relationship between time and concentration. However, before fitting a GAM, the concentration
 184 and accompanying data is checked and processed (Figure 2; “Data Checks and Preparation”) as
 185 follows: The algorithm conducts a preliminary check for the required chamber parameters which
 186 are; id, ordered times of measurement, air temperature (°C), volume, area, and air pressure. In
 187 addition, air temperature is expected to be initially in Celsius, which is automatically converted to
 188 Kelvin during the processing of concentration data in preceding steps. The data is then ordered
 189 based on id and time to maintain correct chronological order of chamber measurements. CH₄ is then
 190 converted from ppm to moles using Ideal Gas Law:

191

$$192 CH_4_{moles} = \frac{(CH_4_{ppm} \times P \times V)}{(R \times T)} \quad (1)$$

193

194 where P is air pressure (Pa), V is chamber volume (m³), R (8.314 J / (mol × K) is the universal gas
 195 constant, and T is air temperature inside the chamber (K). After preliminary data checks and initial

196 processing of the concentration data, the concentration time series is then fit to a GAM (i.e.
197 $\text{gam}(\text{CH4}_{\text{moles}} \sim \text{s}(\text{time}, \text{k} = \text{gam_knots}))$), where the smoothing parameter 'k' is a user defined
198 parameter named 'gam_knots' which has a default value of 5. The value of 'k' cannot exceed 3 times
199 the degrees of freedom for a given concentration time series, or the algorithm defaults to fitting a
200 linear model. The algorithm then checks the R^2 value of the fitted GAM to see if it meets the default
201 conditional value of ≥ 0.99 , if so, it proceeds to calculate fluxes following these steps:

202

203
$$\Delta \text{CH4}_{\text{moles}} = \left[\frac{\text{CH4}(t_2) - \text{CH4}(t_1)}{t_2 - t_1}, \frac{\text{CH4}(t_3) - \text{CH4}(t_2)}{t_3 - t_2}, \dots, \frac{\text{CH4}(t_n) - \text{CH4}(t_{n-1})}{t_n - t_{n-1}} \right] \quad (2)$$

204

205 Where $\Delta \text{CH4}_{\text{moles}}$ is the rate of change, calculated as the quotient of the predicted differences in
206 CH_4 concentration between successive time points. Flux is then calculated between successive time
207 points by:

208

209
$$\bar{F}_{\text{Flux}} = \frac{1}{n-1} \sum_{i=1}^{n-1} \frac{\Delta \text{CH4}}{A} \quad (3)$$

210

211 Where mean flux of the chamber measurement is estimated by calculating flux at each
212 successive time step, where flux is determined by dividing $\Delta \text{CH4}_{\text{moles}}$ by the basal area (A) of the
213 chamber, expressed in (m^2). A plot of the time series and model fit is generated and saved in the file
214 directory defined by the user by setting the parameter 'save_directory' (Figures S1-5). Because
215 fluxes were derived from high-frequency (1 Hz) concentration data fitted using a GAM with a strict
216 acceptance threshold of $R^2 \geq 0.99$, analytical uncertainty in the rate-of-change estimation is
217 negligible. Conventional uncertainty propagation (e.g., based on regression slope error or replicate
218 chambers) is not meaningful in this context because the GAM approach fits a smooth curve through
219 hundreds of data points per deployment, effectively minimizing noise and preventing poor-quality
220 fits from contributing to the final flux values. This ensures that the dominant source of variability in
221 the dataset reflects true environmental heterogeneity rather than analytical error. Furthermore,
222 because the chamber headspace was fully sealed and isolated from external turbulence, wind-
223 induced variability—which often motivates uncertainty corrections—is mechanically removed from
224 the flux calculation process. For these reasons, we report spatial variability (e.g., medians, ranges,
225 and interquartile spread) rather than analytical uncertainty, as it provides a more ecologically
226 relevant representation of flux variability across the catchment.

227 In the cases where the initial GAM fit does not meet the $R^2 \geq 0.99$ condition, the algorithm
228 can follow two pathways (Figure 2). Pathway (1) is a result of the algorithm having detected non-
229 linear concentration increases using BRT, while pathway (2) the algorithm has found the chamber
230 measurement has not met any of the conditional requirements for flux calculations, or more
231 generally stated, there was no measurable concentration increase detected automatically. Both
232 pathways are interactive as the user is prompted to confirm the classification of "ebullition" versus.
233 diffusive data sequences in pathway (1), while in pathway (2) the user confirms there is indeed no
234 concentration increase by reviewing the diagnostic plots (see Supplemental text and Figures S2-S6).
235 Once confirmed, the user initiates flux calculations by manually entering the time range of the
236 measurement that should be fitted (Figure 2). "Ebullition" in the context of the algorithm refers to a

237 sudden, non-linear CH_4 increases identified by the algorithm, which likely includes ebullitive events,
238 but does not strictly infer all fluxes calculated this way were from bubbles entering the chamber.

239 2.4 Lake and Stream Metabolism

240 In 2024, we calculated the metabolic parameters net ecosystem production (NEP), gross
241 primary production (GPP), and ecosystem respiration (ER) of oxygen for the lake and streams using
242 dissolved oxygen (DO) collected at a one-minute frequency during chamber measurements (DO
243 sensor accuracy: $\pm 0.1 \text{ mg L}^{-1}$; resolution 0.01 mg L^{-1}). Including metabolic parameters as predictors
244 in the BRT models gave us an understanding of the role microbial oxygen production plays in
245 regulating or not CH_4 emissions from water. DO saturation was adjusted using temperature-
246 dependent solubility constants (Garcia & Gordon, 1992). Oxygen flux at the air-water interface was
247 determined using wind derived gas exchange coefficients and adjusted for water temperature (Cole
248 & Caraco, 1998). NEP was calculated as the rate of change in DO concentration over each chamber
249 deployment, adjusted for air-water exchange (Hall & Madinger, 2018; Noss et al., 2018). GPP and ER
250 were partitioned from NEP by applying a threshold of $200 \text{ } \mu\text{mol m}^{-2} \text{ s}^{-1}$ photosynthetically active
251 radiation (PAR), which distinguishes intervals with effective photosynthesis from those with
252 negligible light-driven production, despite continuous daylight during Arctic summer. Aggregating
253 each chamber DO measurement into one-minute intervals, we calculated mean NEP, GPP, and ER for
254 each chamber placement (Winslow et al., 2016). While this methodology is sound for the lake, there
255 is some caveats in relation to stream metabolism. Because we are using a model which assumes
256 wind driven gas exchange for small streams, we likely underestimate gas exchange in parts of the
257 streams where turbulence from streambed roughness dominates. Nonetheless, the approach
258 captures broadly the metabolic trends in lake and stream metabolism observed in other Arctic and
259 Boreal waterbodies (Mulholland et al., 2001; Rocher-Ros et al., 2021; Ayala-Borda et al., 2024; Klaus
260 et al., 2022; Myrstener et al., 2021) and is useful for comparing fluxes across aquatic biomes.

261 2.5 Spatial Flux Evaluation

262 We uploaded as a spatial layer in QGIS version 3.40.1 (QGIS Development Team, 2025) an
263 orthomosaic image produced by Airbus satellite Pléiades 1B and the chamber placements as points
264 with their associated flux estimates. We spatially analyzed the CH_4 fluxes by creating bi-weekly
265 emission heatmaps using the Kernel Density Estimation (KDE) algorithm in QGIS. The use of KDE
266 allowed us to smooth across discrete chamber measurements, yielding an intuitive continuous
267 surface representation of CH_4 flux hotspots and their evolution through time (Figure 2). We set the
268 radius to between 30-35 meters to allow some connectivity between points which allows for a
269 smooth representation of any environmental gradients that might be captured. We used the default
270 method using a quartic kernel shape weighted by the flux calculated for each chamber placement.
271 While “ebullitive” fluxes were not considered in further statistical analysis (i.e., in the BRT), those
272 fluxes are depicted in the resulting heatmaps. Overall, using KDE allowed for an intuitive
273 interpretation of the seasonal and spatial development of flux hotspots in the research area.

274 We additionally compared daily CH_4 emissions from Sanningasup Tasia catchment relative to
275 other Arctic-Boreal Lake classes compiled in the Boreal-Arctic Wetland and Lake Dataset (Kuhn et al.
276 2021; Olefeldt et al., 2021). A Kruskal-Wallis test was performed to determine significant differences
277 ($p < 0.05$) in the log transformed daily fluxes from Sanningasup Tasia ($n = 48$) and its streams ($n = 35$)
278 relative to broader biome-scale fluxes from Small Peat Lakes ($n = 50$), Medium Peat Lakes ($n = 36$),
279 Large Lakes ($n = 10$), and Small Yedoma Lakes ($n = 7$). We then performed pairwise Wilcoxon rank-
280 sum tests with Benjamini-Hochberg adjustment for multiple comparisons to highlight specific
281 contrasts between Sanningasup Tasia catchment and the other lake classes. Conducting this

282 provides an understanding of how Sanningasup Tasia catchment emissions compares to other Arctic
283 waterbody types.

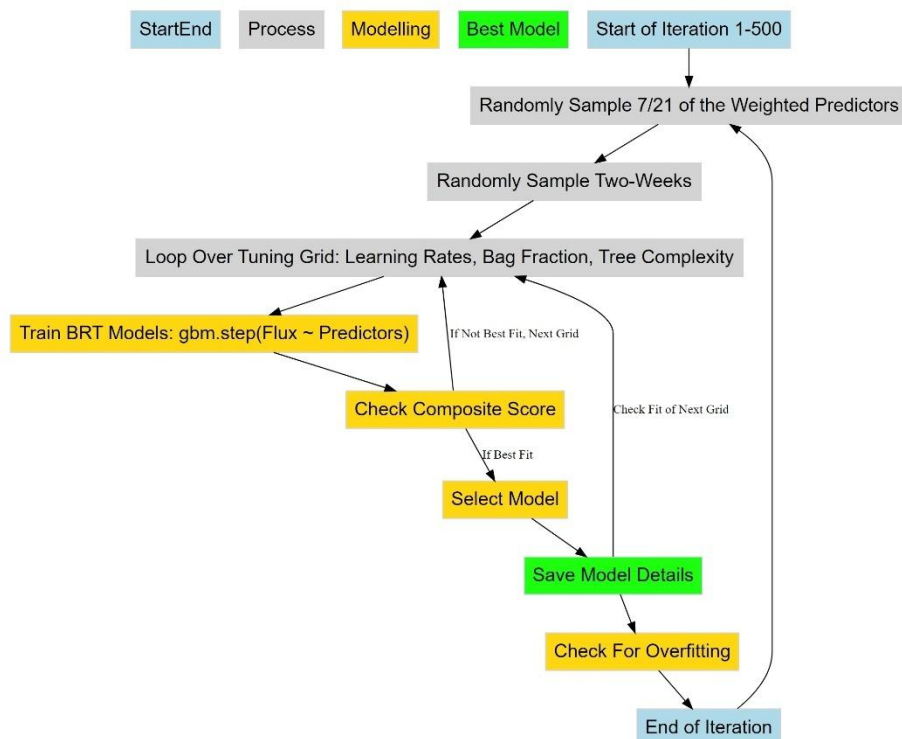
284 2.6 Decoding Methane Drivers

285 To determine important drivers and their partial effects on diffusive CH₄ fluxes, we trained
286 BRT with physicochemical water parameters, catchment soil temperatures, catchment soil moisture,
287 surface air temperatures, local meteorology, and Julian day (Figure 3). Considering we only collected
288 water temperature in 2023, we used flux data from 2024 for training the BRT. We have focused on
289 diffusive fluxes due to the unpredictability of fluxes when “ebullitive” processes were considered in
290 the models. The diffusive fluxes give us a detailed view of environmental controls shaping CH₄ fluxes
291 coming from the catchment. To characterize fluxes we assembled a comprehensive set of predictors
292 including; (a) aquatic variables measured *in-situ* with a water sonde at each chamber deployment
293 (e.g., Conductivity (µS/cm), pH, redox potential (mV), dissolved oxygen (mg/L), oxygen saturation
294 (%), water temperature (°C), and fluorescent dissolved organic matter (FDOM; RFU)) (Figure S7), (b)
295 catchment soil characteristics collected at nearby climate stations (e.g., soil volumetric water
296 content at 10 cm and soil temperature at 40 cm), and (c) meteorological variables collected from a
297 nearby climate station (e.g., Surface air temperature at 2 cm (°C), Air temperature (°C), relative
298 humidity (%), air pressure (mbar), precipitation (mm), PAR (µmol m⁻²s⁻¹), and mean wind speed (ms⁻¹)
299 and direction (°)). Lake water levels (mm) were included to characterize the effect of changing
300 hydrologic conditions and its influence on lake CH₄ fluxes. Although water depth was recorded
301 during chamber deployments using the AquaTroll 600, it was not included as a predictor in the BRT
302 models. In shallow Arctic lakes like Sanningasup Tasia (<4.5 m), CH₄ is primarily sediment-derived,
303 with deeper zones more likely to promote oxidation or dilution due to greater oxygen exposure
304 (Bogard et al., 2014; Bulínová et al., 2025; Emerson et al., 2021; Li et al., 2020). Shoreline fluxes
305 often dominate due to anoxic, vegetated sediments, while interior zones tend to suppress emissions
306 (Thompson et al., 2016; Kyzivat et al., 2022; Rasilo et al., 2015). We therefore prioritized
307 biogeochemical water column predictors—FDOM, dissolved oxygen saturation, and GPP—over
308 depth (Christiansen et al., 2015; Singleton et al., 2018), and explicitly captured depth gradients via
309 boat-based chamber deployments across the lake interior. Catchment soil characteristics were
310 included to capture the hydrogeological conditions surrounding the catchment. We used catchment
311 soil temperature at 40 cm to represent subsurface active-layer conditions that influence deeper
312 thermal dynamics, groundwater inflow, and delayed soil heat retention through the thaw
313 season. Soil volumetric water content (VWC) at 10 cm was included to gain an understanding if
314 dryer, or wetter catchment conditions effect surface water CH₄ fluxes, and to act as a substitute for
315 water level in the lake early in the season as these two share a Pearson’s correlation of $r = 0.93$.
316 Additionally, we used VWC at 10 cm depth because it was the most complete and continuous
317 dataset across the measurement depths, and highly correlated with VWC at 20 cm, 30 cm and 40
318 cm. To reduce multicollinearity amongst the predictors, we set up weighting for random feature
319 selection by calculating the average absolute Pearson correlations between predictors and assigning
320 weights inversely proportional to the correlations, resulting in higher weights given to predictors
321 with decreased collinearity and thus more likely to be included as a predictor.

322 Using the “gbm.step” algorithm from the R package “dismo” version 1.3.14 (Elith et al.,
323 2008; Hijmans et al. 2023), we iteratively attempted to fit 500 BRT with a subset of randomly
324 sampled two-week time series of flux calculations and 7 of the 21 weighted predictors. Each two
325 weeks must have at least 90 observations, or the date range is buffered on either end of the time
326 series to meet the minimum observation requirement. The algorithm uses 10-fold cross-validation to
327 minimize overfitting the models (Elith et al., 2008). If a randomly sampled two weeks did not meet

328 the minimum required observation of 90, the time series was buffered on both ends of the date
329 range to meet the minimum required observations. BRT were optimized using a grid search where
330 hyperparameters such as learning rate (0.001, 0.002, 0.003, 0.004, 0.005), tree complexity (1, 3, 5,
331 7), and bag fraction (0.30, 0.40, 0.50), were tuned for each model fit. While bag fraction values in the
332 range of 0.5–0.8 are more commonly used, a lower bag fraction increases stochasticity in tree
333 construction, which helps reduce overfitting—especially important for modeling noisy and highly
334 non-linear CH₄ flux data. This conservative approach favors identifying robust general patterns
335 rather than fitting noise or outliers. Variable monotonicity was handled dynamically for each subset
336 of predictors using Spearman's rank correlation. Monotonicity for categorical variables was set to
337 zero, while positive correlations were given a +1 and negative correlations were given a -1. The
338 model with the best composite score was selected for each iteration. The composite score was
339 calculated by adding together the standardized cross-validation error, standardized correlation
340 error, and the cross-validation correlation. The model was finally saved after checking for over fitting
341 by taking the difference between cross validated mean deviance and training mean deviance and
342 dividing the difference by training mean deviance. Because the inherently noisy nature of ecological
343 data, we allowed for 40% difference between cross validated predictions and training data. We
344 further calculated the percent deviance explained for each BRT model using the formula: % deviance
345 explained = 100 × ((null deviance – residual deviance) / null deviance), where the null deviance
346 represents the deviance of a model using only the mean response, and the residual deviance is from
347 the fitted BRT model. Each fitted model and its metadata were saved for further analysis. This
348 modelling structure ensures robustness against outliers and ensures data integrity through
349 dynamically handling monotonicity and applying overfitting constraints. Furthermore, the structure
350 ensures robust predictions of fluxes by accounting for multi-collinearity amongst predictors and flux
351 heterogeneity throughout the season.

352 To visualize the results of the models, we plotted partial dependence two ways. First, we
353 extracted partial dependence information for understanding model structure, i.e., those predictors
354 and interactions which were used to split trees and decrease cross validated prediction error. In
355 addition, we made isolated predictions for each environmental feature in the model by holding all
356 other predictors at their median to gain a more mechanistic understanding of which conditions
357 and/or processes are directly affecting CH₄ fluxes. The two ways of visualizing partial dependence
358 give us an ecological understanding of how integrated direct and indirect effects regulate fluxes from
359 the catchment, but also how individual variables and/or processes regulate fluxes from the water
360 surfaces, respectively. All visualizations were generated using the R package “ggplot2” version 3.5.0
361 (Wickham, 2016), and the package “DiagrammeR” version 1.0.11 for flowcharts (Iannone, 2024).



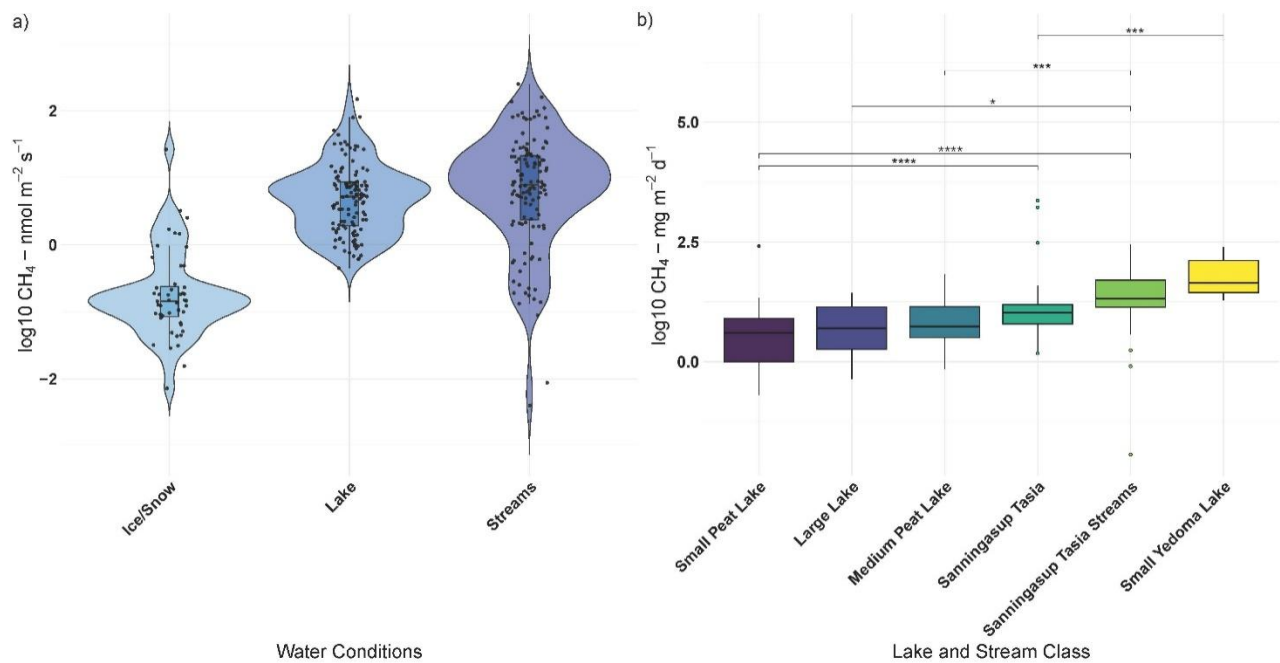
364 Figure 3. Workflow of the iterative randomized process for selecting the best BRT for predicting
 365 diffusive CH₄ fluxes using various environmental predictors. Blue boxes represent the start and end
 366 of a single iteration through an index of weighted predictors, time periods, and tuning grid (grey
 367 boxes). Yellow boxes represent the model selection logic, while the green box represents the storage
 368 of flux predictions and selected model details for the included predictors and two-week sub-sample
 369 of chamber measurements.

370 3 Results and Discussion

371 3.1 Overview

372 Methane fluxes from permafrost affected catchments are influenced by a complex interplay
 373 between climatological, hydrogeological, and biogeochemical processes. This study highlights the
 374 transient nature of CH₄ fluxes from a permafrost catchment in west central Greenland and the
 375 partial effects of physiochemical water conditions, local meteorology and catchment conditions
 376 (Figures 4-7). CH₄ emissions from the catchment were variable across water conditions, with streams
 377 exhibiting the highest emissions (Figure 4). In comparison to the global coverage of the Boreal-Arctic
 378 Wetland and Lake Dataset (Olefeldt et al., 2021), besides small peat lakes, daily fluxes from
 379 Sanningasup Tasia at 8.3 mg m⁻² d⁻¹ were mostly comparable to other permafrost waterbodies across
 380 the Arctic-Boreal region, which ranges between 3.8-5.4 mg m⁻² d⁻¹ (Figure 4). Highlighting the
 381 importance of emissions from small streams, Sanningasup Tasia streams showed significantly higher
 382 daily fluxes (18.2 mg m⁻² d⁻¹) than all inland water body classes, except Yedoma lakes (43.7 mg m⁻² d⁻¹). Our results indicate that CH₄ fluxes were seasonally variable and controls on fluxes shifted from
 383 hydroclimatic factors during colder periods to biogeochemical processes as the catchment warmed
 384 and increased in productivity (Figure 3-4 and Figure A1). The seasonal thaw of annual snow and ice
 385 accumulation in the two study years varied in timing and duration due to 2023 staying anomalously
 386 snowy until the beginning of July, where in 2024 the number of snow free days aligned with
 387 historical records. In 2023, our initial chamber measurements between July 03-15 captured peak
 388

389 median fluxes at $8.9 \text{ nmol m}^{-2} \text{s}^{-1}$ just as the ice began to break on the lake. In an effort to capture
 390 similar conditions in 2024, we used an index of historical snow free days on the island which led to
 391 us capturing median fluxes of $0.18 \text{ nmol m}^{-2} \text{s}^{-1}$ between May 24-June 05 atop ice and snow. Peak
 392 median fluxes of $8.1 \text{ nmol m}^{-2} \text{s}^{-1}$ in 2024, were comparable to 2023, but occurred a month earlier
 393 between June 11-19. As runoff water receded and the catchment warmed, growing season
 394 commenced in conjunction with steadily decreasing median fluxes between 3.9 and $4.5 \text{ nmol m}^{-2} \text{s}^{-1}$.
 395 This study further provides methods to disentangle important drivers and their partial effects on CH_4
 396 fluxes using BRT (Figure 3-4). In general, CH_4 fluxes were strongly dependent on discrete oxic-anoxic
 397 aquatic environments under the chamber (Figure 4 and Figure A1). This research emphasizes the
 398 importance of integrating field measurements with GIS-based spatial analysis to monitor CH_4 fluxes
 399 in permafrost catchments. It further drives home the importance of seasonal transition periods in
 400 predicting fluxes from Arctic waterbodies.

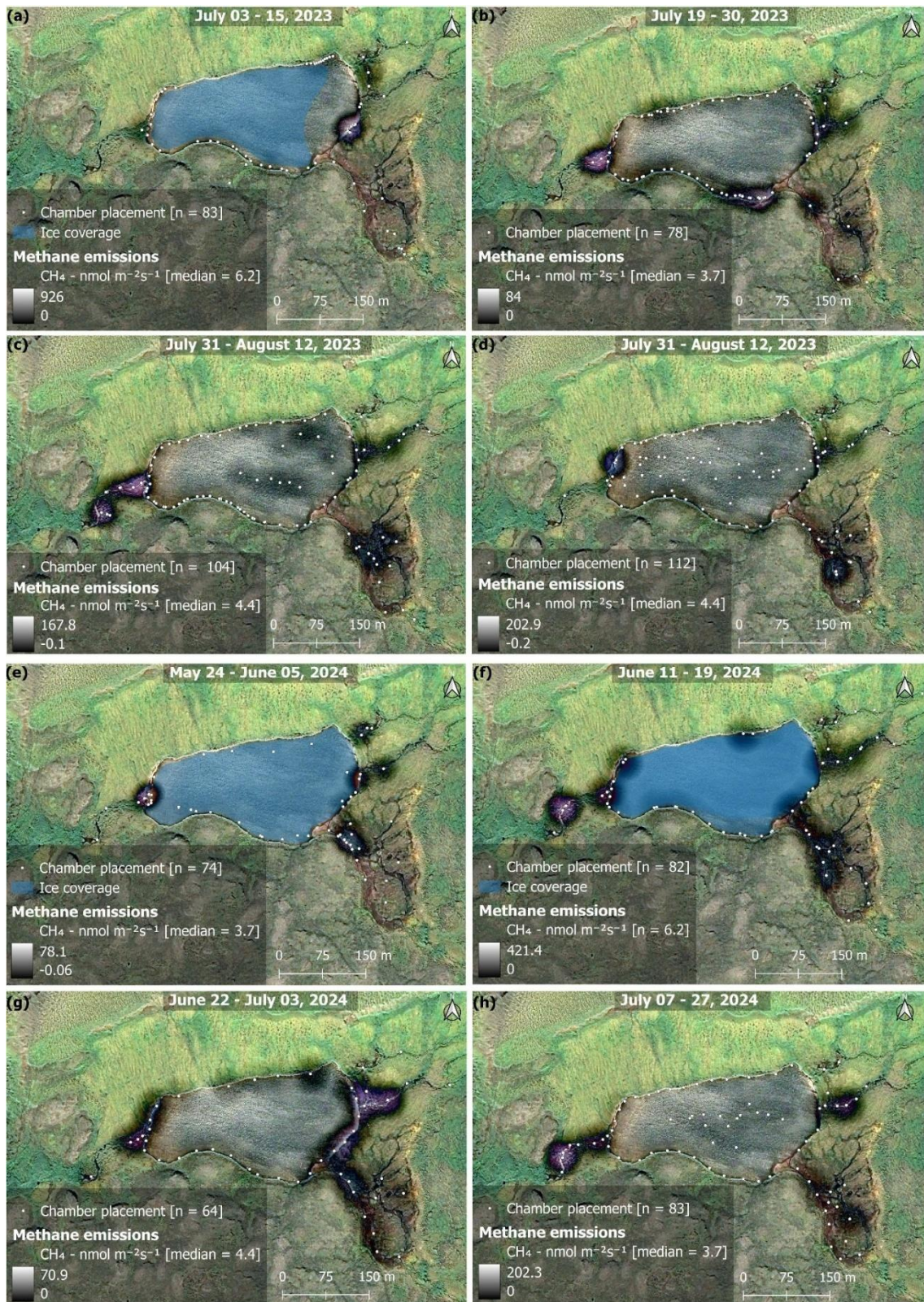


401
 402 Figure 4. Panel a) shows log transformed CH_4 fluxes across the different catchment water conditions
 403 during 2024 field season and b) compares log transformed daily CH_4 fluxes (y axis) between
 404 Sanningasup Tasia catchment and other permafrost waterbodies (Kuhn et al., 2021) across the
 405 Arctic-boreal region. Connecting brackets and stars show, for example, that Sanningasup Tasia had
 406 significantly ($p < 0.05$) higher daily emissions when compared to Small Peat Lakes, while daily
 407 emissions from Sanningasup Tasia Streams were significantly higher than all lake classes except
 408 Yedoma Lakes.

409 3.2 Spatial and Temporal Evolution of Methane Fluxes

410 In both 2023 and 2024, spatial and temporal evolution of fluxes occurred somewhat
 411 heterogeneously in the catchment, but generally “hotspots” occurred in the streams and where they
 412 enter the lake (Figure 5 a-b, e-f). Despite different time periods of the thaw, fluxes in the catchment
 413 in both years followed a similar trajectory, with peak fluxes occurring post thaw and decreasing
 414 through the growing season. In 2023, snow persisted anomalously late into the summer season, and
 415 soil temperatures were the coldest recorded in a 6-year record (Figure S8). We found that local
 416 climate and catchment soil characteristics were at times, (i.e., during the thaw season and towards
 417 the peak of growing season) more important than water temperature in predicting 2023 fluxes,
 418 suggesting catchment contributions to surface waters plays an indirect role in CH_4 fluxes (Figure S9).

419 While water temperature was found to be relatively important in both years, catchment CH₄ fluxes in
 420 2024 suggest the system is more driven by variability in dissolved organic matter and microbial
 421 production of oxygen (Figure 4-7 and Figure A1).



422

423 Figure 5. Maps showing the bi-weekly spatial evolution of CH₄ emissions during 2023 (a-d) and 2024
 424 (e-h). The time period covered in each map is given at the top of each map. Whiter colors represent

425 areas of high emissions, while darker, or no color represent areas of lower, or no emissions (see
426 color bars in map legends). Areas outside of the water were not measured and are artifacts from the
427 KDE mapping algorithm interacting with the image (i.e., purple color = no data). Each white point on
428 the map represents the placement of the floating chamber. Orthomosaic background image © CNES
429 (2024), Distribution Airbus DS, produced from Pléiades 1B satellite imagery.

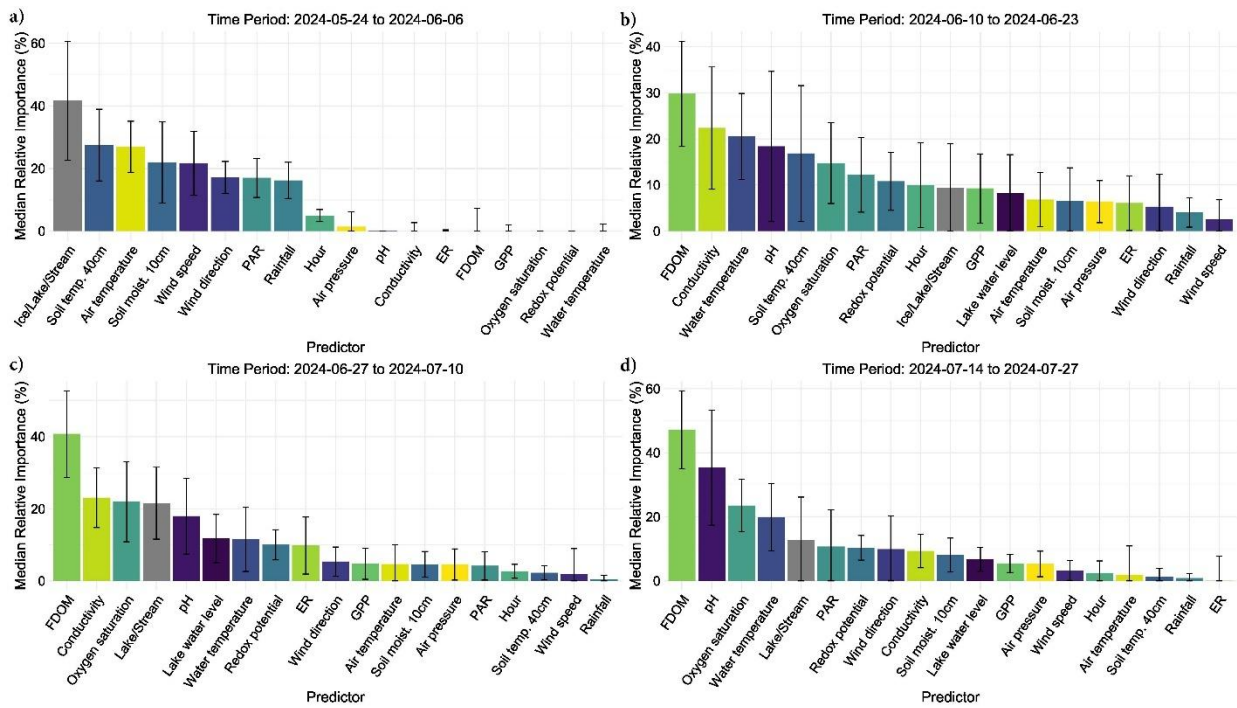
430 The main inlet to the lake is a warm spring with median temperatures of 7.4 °C and tended
431 to be a persistent location throughout the season for increased CH₄ fluxes. The warm spring area in
432 the southeast is a complex area where a perennial spring bubbles out of the ground forming a
433 perennial tributary to the lake. However, the spring seeps out along the base of the hillslope to the
434 east, subsequently forming a peat fen environment (Figure 5). The eastern most inlets are fed by
435 meltwater flowing through the vadose zone, but also served as a persistent location for increased
436 CH₄ fluxes. Fluxes from inlet streams followed along an upland-wetland environmental gradient,
437 where fluxes at the headwaters of streams were generally close to 0, or slightly taking up CH₄, but
438 steadily increased as steeper upland slopes gave way to more gradual water saturated slopes and
439 pooling sediments. This is consistent with previous work on the island showing CH₄ fluxes association
440 with soil microbial assemblages shifting from methanotrophic to methanogenic along an upland-
441 wetland gradient, respectively(Christiansen et al., 2015). Additionally, the catchment serves as
442 micro-topography previously described as an area of snowmelt retention, and subsequently an area
443 of nutrient and/or dissolved organic matter pooling (Westergaard-Nielsen et al., 2020), which has an
444 impact on CH₄ fluxes throughout the season (Figure 7). While high fluxes were recorded along the
445 shore and in the open water of the lake, fluxes tended to be patchy and decreased moving away
446 from the inlet streams (Figure 5 and Figure S10). However, as soon as the lake water flowed to the
447 outlet, fluxes increased substantially. As the summer season progressed, CH₄ fluxes declined across
448 most of the catchment, becoming largely confined to the warm spring inlet and the eastern inlet
449 streams (Figure 5). Field observations of late-season fluxes in 2024, found decreased fluxes were
450 associated with submerged filamentous green algae in stream channels, while assemblages of iron-
451 oxidizing bacteria on the stream banks were associated with increased fluxes, (Figure A2). The
452 spatial and temporal evolution of fluxes was driven by seasonally shifting environmental conditions.

453 3.3 Boosted Regression Tree Results

454 Out of 500 iterations, 321 BRT were fit, and showed good alignment and consistently
455 performed well in cross-validation, with a correlation median of 0.40 between observed and
456 predicted values, and a median deviance standard error of 131. Between 8.4% and 62.4% with a
457 median of 27.3% of the CH₄ flux variability was explained by the various models and included
458 environmental conditions, suggesting a substantial proportion of CH₄ fluxes were explained by the
459 environmental conditions included. The calculated root mean squared error (RMSE), which reflects
460 the average magnitude in prediction error of the BRT, ranged between 6.5 to 28 nmol m⁻²s⁻¹, with a
461 median of 13.7 nmol m⁻²s⁻¹. The summary statistics reflect models that performed reliably and with
462 fairly good accuracy in predicting diffusive CH₄ fluxes from the catchment in 2024. The models
463 predicted shifting relative importance (Figure 6) and partial effects of the various environmental
464 conditions throughout the season (Figure 7). The magnitude of CH₄ fluxes predicted by the BRT
465 models were strongly influenced by localized biogeochemical conditions within the water column
466 based on whether the flux was originating from the lake, stream, or if it was influenced by ice or
467 snow (Figure 4-7, and Figure A1a-d). Visualizing partial dependence of predictors important for
468 model structure, revealed integrated ecological effects between local meteorology, catchment
469 conditions and physiochemical water conditions (Figure 7). However, isolated direct marginal effects
470 of the various environmental conditions suggest fluxes from water surfaces are directly regulated via

471 biochemical processes associated with GPP and ER of oxygen (Figure A1b-d). Areas with violet, or
 472 purple colors are a result of the heatmap interacting with the aerial image.

473



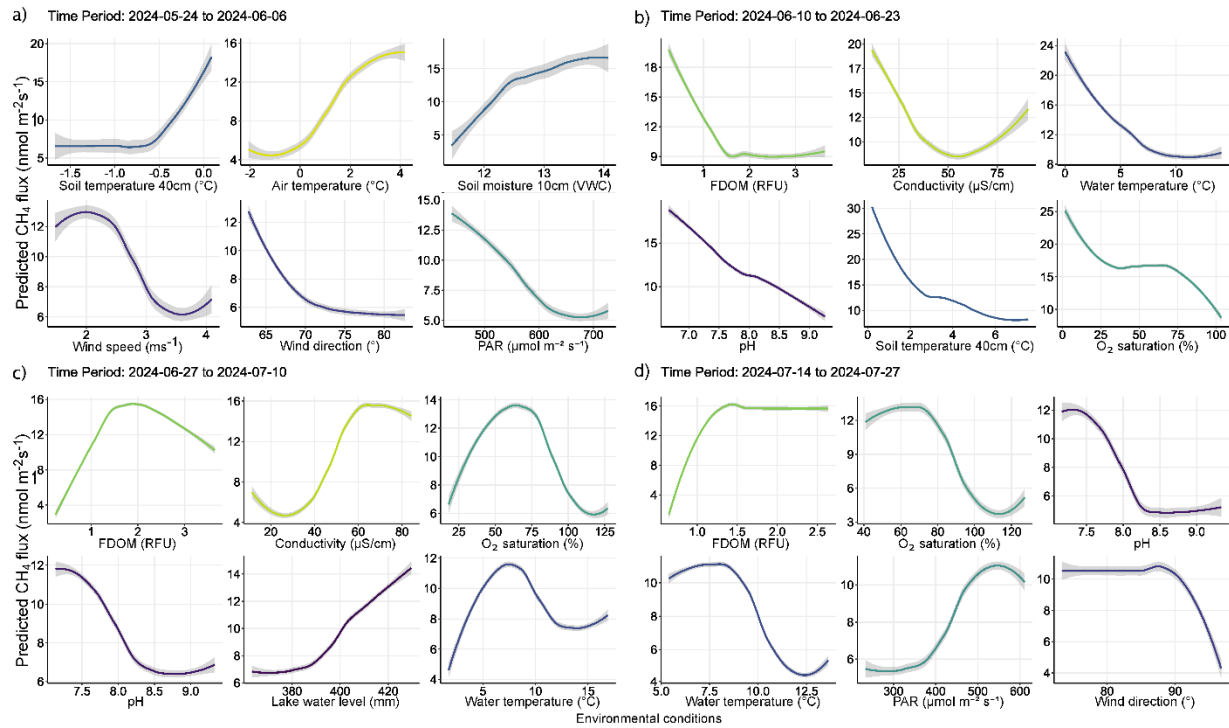
474

475 Figure 6. Bar charts show the relative importance of environmental conditions predicting diffusive
 476 CH₄ fluxes using bar-plots and standard error bars. Each predictor variable is on the x-axis, while its
 477 percent importance for its inclusion in a fitted BRT is given on the y-axis where the standard error
 478 bars represent variability in importance based on presence or absence in a given model. Each bar
 479 color represents a distinct environmental condition.

480 3.3.1 Spring Thaw Phase: Peak Fluxes Driven by Hydrological and Climatic Controls

481 The spring thaw phase marks a shift in catchment conditions, where a frozen landscape gives
 482 way to thaw season and hydro-connectivity between land and water is strong (Figure 5c-d, g-h). In
 483 the spring thaw phase, initial peak fluxes of CH₄ were primarily dependent on increasing rainfall,
 484 changing wind conditions, warming air and soil temperatures, and increased soil moisture content,
 485 while low dissolved organic matter (i.e., FDOM) indicated increased fluxes (Figure 6a-b and 7a-b).
 486 Soil moisture was found to have a Pearson's $r = 0.93$ with lake water levels, suggesting the lake levels
 487 are strongly connected to snowmelt and groundwater hydrology (Figure S11). The distribution of
 488 nutrients on the island has been shown to be linked to snowmelt and hill slope topography
 489 (Westergaard-Nielsen et al., 2020), which is likely playing a role during the early part of the season,
 490 but especially later in the year as DOM, a proxy for nutrients, becomes the primary limiting factor in
 491 predicting higher fluxes (Figure 7b-c) (Olid et al., 2021, 2022). The processes driving CH₄ fluxes from
 492 water surfaces is likely two-fold.

493



494

495 Figure 7. Partial dependency plots illustrating the indirect and direct marginal effects of various
 496 environmental conditions predicting diffusive CH₄ fluxes. Each panel displays the effect of a
 497 numerical predictor used during model training to predict CH₄ fluxes. Although some predictors may
 498 not have been directly involved in regulating fluxes from water surfaces, their evaluation reveals the
 499 relationship between water column conditions and catchment processes regulating CH₄ fluxes. The
 500 figures are ordered by importance in each time period and the colors correspond to those seen in
 501 Figure 6. The colored lines represent the result of a fitted general additive model ($y \sim s(x)$) and thus
 502 a smooth representation across the 321 fitted BRT models. The grey shaded area around the line
 503 represents $\pm SE$ (0.02 - 0.2). Each predictor and its numerical range are given on the x-axis, while
 504 predicted fluxes are given on the y-axis.

505 As snowfall turned to rain, the thawing of soils accelerated and water content in the active
 506 layer increased, potentially driving peak emissions via the lateral mobilization of dissolved CH₄
 507 toward surface waters (Figure 7a-b) (Walter Anthony et al., 2012; Neumann et al., 2019; Olid et al.,
 508 2022). However, as the thaw progressed, contributions to fluxes from catchment soils decreased as
 509 the upper layers began to dry and lake water levels reached their maximum (Figure 7b-c). DOM
 510 serves as a critical substrate for both CH₄ production and oxidation, particularly in permafrost-
 511 influenced regions where thawing can release large amounts of particulate matter (Keskitalo et al.,
 512 2021; Bouranis et al. 2025). Anaerobic conditions in water saturated soils and low oxygenated
 513 waters may have further driven fluxes during the thaw period as methanogenic microbial
 514 communities rapidly consumed incoming labile organic compounds (Neumann et al., 2019;
 515 Stevenson et al., 2021). However, as the thaw progressed, the lake briefly shifted to net-autotrophy
 516 (Figure S6), marking an important shift from hydroclimatic controls on fluxes, to a patchwork of
 517 biochemical transport pathways and barriers (Figure 7 b-d and Figure A1b-d). During this transition,
 518 increased GPP and the resulting oxygen saturation in the lake and streams enhance methanotrophic
 519 activity, thereby promoting methane oxidation and reducing net CH₄ emissions (Figure 7b-c and
 520 Figure A1b-c). The central role of oxygen availability and active methanotroph communities in
 521 regulating methane fluxes during Arctic thaw has been demonstrated in both tundra landscapes and

522 permafrost mires (Christiansen et al., 2015; Graef et al., 2011; Singleton et al., 2018). As oxygen
523 production increases, greater amounts of oxygen become available to support methanotrophic
524 activity in the water column. Methanotrophic activity is likely represented in the observed reduction
525 of CH₄ fluxes during periods of decreased ER (i.e., when oxygen consumption is elevated, Figure A1c),
526 as higher oxygen availability enhances aerobic methane oxidation (Figure 7c). However, the streams
527 remain net heterotrophic despite increasing GPP and ER during this time period, therefore providing
528 a more suitable environment for CH₄ production and flux (Figure S6). Thus, the lake and streams
529 reflect distinct ecosystems for the production and flux of CH₄, where the lake being an overall
530 methane source, has a greater tendency to oxidize CH₄ following the thaw, while the streams follow
531 along a low-to-high flux gradient as the slope flattens and soils become saturated (Westergaard-
532 Nielsen et al., 2020; Stevenson et al., 2021).

533 3.3.2 Growing Season: Oxic-Anoxic Transport Pathways and Barriers

534 Early in the growing season the lake and streams enter into a transition phase, where peak
535 fluxes become increasingly dependent on biochemical pathways related to DOM availability,
536 conductivity, oxygen saturation and pH (Figure 7c). DOM is the limiting factor late in the season
537 where higher fluxes are increasingly dependent on water column conditions with greater levels of
538 DOM (Figure 6c-d and 7c-d). CH₄ fluxes during this time period were strongly associated with
539 indicators of microbial activity forming oxic-anoxic transport barriers, or pathways, respectively. For
540 example, microbial activity in anoxic sediments maybe producing CH₄, but whether it is diffused to
541 the atmosphere is directly affected by the micro-conditions of the water column (e.g., DOM,
542 conductivity, pH, and/or GPP/oxygen saturation), either forming an oxidative barrier, or an anoxic
543 pathway (Figure 7c-d and Figure A1). For example, groundwater transport of CH₄ from anoxic
544 sediments to oxygen-rich streams may result in water with high concentrations of both. While some
545 of the CH₄ is likely oxidized during transport, it can be that both are respiration at turbulent sections of
546 the stream, which were the highest fluxes observed from the streams and during this phase of the
547 season (Street et al., 2016; Neumann et al., 2019; Olid et al., 2022; Kleber et al. 2025).

548 Fluxes are further affected by water conditions either favoring methanogenic, or
549 methanotrophic activity (Conrad, 2007; Cunada et al., 2021; Emerson et al., 2021). pH levels near
550 neutral likely indicate water conditions favorable to methanogenesis at the sediment-water
551 interface, while increasing alkalinity may reduce methanogenic and/or favor increased
552 methanotrophic activity as growing season progresses (Figure 7c-d). For example, during growing
553 season micro-pH and oxygen saturation conditions in the lake and streams are influenced by the
554 ever-increasing presence of macrophytes, mosses and plankton, which tend to drive pH and oxygen
555 levels higher (Liebner et al., 2011; Cunada et al., 2021). Here we show that increasing pH and oxygen
556 saturation, as a result of primary production, create an aerobic environment that favors
557 methanotrophic activity, thereby driving CH₄ emissions down through the growing season (Figure
558 7c-d, Figure A1). Declines in oxygen saturation driven by microbial respiration can create anoxic
559 conditions that enable CH₄ emissions from sediment to surface waters (Conrad, 2007; Michel et al.,
560 2010; Street et al., 2016; Cheng et al. 2024). Such a mechanism likely explains the formation of flux
561 hotspots associated with decomposing iron-oxidizing bacterial mats along stream banks (Figure A2)
562 (Wallenius et al., 2021; Cheng et al. 2024). In the case of the bacterial mats, we observed fluxes
563 were highest in the streams where bacterial assemblages had become exposed to the atmosphere
564 and were decomposing in stagnant water (Figure A2), which may suggest that the decomposition of
565 the bacteria was releasing dissolved organic substrates in a low-oxygen environment already primed
566 for methanogenic activity (Wallenius et al., 2021; Cheng et al. 2024). This idea is supported late in
567 the season when increased CH₄ emissions become dependent on niche environments where

568 moderate levels of dissolved organic matter (FDOM) and low oxygenated water predict higher fluxes
569 (Figure 7d and Figure A1d). However, submerged bacterial mats along with filamentous green algae
570 the presence of macrophytes and/or mosses in the lake and streams, were associated with lower
571 fluxes, suggesting they form oxidative barriers for CH₄ fluxes from the sediment when submerged
572 (Figure 7d and Figure A1d) (Heilman & Carlton, 2001; Laanbroek, 2010; Liebner et al., 2011; Esposito
573 et al., 2023). The submerged, or not status of bacterial assemblages' points to an interesting
574 feedback mechanism between CH₄ fluxes and dropping water levels creating variability in emission
575 pathways. Similar processes have been shown in relation to submerged brown mosses in Arctic
576 tundra ecosystems have been shown to promote CH₄ oxidation and thus decrease CH₄ emissions
577 from sediments (Žárský et al., 2018). Overall, these results highlight the broader importance of fine-
578 scale biogeochemical dynamics shaping CH₄ fluxes from a permafrost catchment and provide an
579 important data point in an uncertain region of the world.

580 4 Conclusion

581 This research provides a temporally resolved catchment scale CH₄ flux analysis across
582 different waterbody types and conditions—lake, streams, and ice/snow-covered surfaces—
583 subsequently describing important biogeochemical and climatic controls on emissions. Often lost in
584 temporally coarse assessments is a detailed understanding of seasonal transitions in processes
585 related to CH₄ fluxes and environmental control mechanisms. Leveraging BRT to fit hundreds of
586 randomized models and visualizing the direct, and indirect controls on CH₄ fluxes reveals variability
587 in how, for example, DOM and/or water temperature affect fluxes differently as the Arctic summer
588 progresses. We presented an approach which captures ecosystem-scale effects, but furthermore
589 describes isolated mechanistic effects related to, for example, GPP, revealing that primary
590 productivity plays a critical role in regulating CH₄ emissions from permafrost affected waterbodies.
591 This work contributes to understanding carbon feedback mechanisms in a region where process-
592 level knowledge is needed to scale global models simulating CH₄ emissions from permafrost affected
593 waterbodies.

594 Code Availability

595 R code for calculating methane fluxes can be found here: <https://github.com/mthayne527/fluxCH4>.

596 Data Availability

597 Meteorlogical can be accessed here: <https://doi.org/10.17897/FEGK-0632>, and soil data here:
598 <https://doi.org/10.17897/6G78-P793>, <https://doi.org/10.17897/9N7Z-GA63>, and can be
599 accessed via the Greenland Ecosystem Monitoring website: <https://data.g-e->
600 [m.dk/datasets?theme=climate](https://data.g-e-.dk/datasets?theme=climate). BAWLD circum-Arctic waterbody dataset can be found here: DOI:
601 10.5194/essd-13-5151-2021. Water chemistry and chamber data can be requested from Torsten
602 Sachs at Helmholtz Centre for Geosciences in Potsdam, Germany (GFZ).

603 Author contributions

604 MWT collected, compiled and analyzed data, and wrote the manuscript. KK contributed to
605 collecting, compiling, and analyzing data and writing parts of the manuscript. CW contributed to
606 methodological guidance and providing feedback and writing parts of the manuscript. AK
607 contributed to providing comments, feedback, and guidance on interpreting results and writing
608 various parts of the manuscript. TS contributed to collecting data, providing comments, feedback,
609 and guidance on interpreting results and writing the manuscript.

610 Competing interests

611 The authors declare that they have no conflict of interest.

612 Acknowledgments

613 This research is part of the MOMENT project which is funded by the Federal Ministry of
614 Research, Technology and Space (BMFTR) under grant number 03F0931E. We acknowledge the
615 community of Qeqertarsuaq, Greenland for allowing us to research their land and water. We
616 acknowledge the help received from all of the partners of the MOMENT project, with a specific
617 acknowledgment for Selina Undeutsch and Prof. Dr. Lars Kutzbach from the University of Hamburg.
618 We acknowledge Dr. Evan Wilcox for collecting water level from the lake during the 2024 field
619 season. We would acknowledge the University of Copenhagen and the Arctic Station team for
620 providing an environment for conducting this research. We acknowledge the work of the Greenland
621 Ecosystem Monitoring network and specifically Charlotte Sigsgaard for her help in getting
622 meteorological and soil data. ChatGPT models 4.1 and 5 were used to edit parts of the manuscript.

623 References

624 Ayala-Borda, P., Bogard, M. J., Grosbois, G., Preskienis, V., Culp, J. M., Power, M., and
625 Rautio, M.: Dominance of net autotrophy in arid landscape low relief polar lakes, Nunavut,
626 Canada,

627 Bastviken, D., Cole, J. J., Pace, M. L., and van de-Bogert, M. C.: Fates of methane from
628 different lake habitats: Connecting whole-lake budgets and CH₄ emissions, *J. Geophys. Res.-*
629 *Biogeosci.*, 113, G02024, <https://doi.org/10.1029/2007JG000608>, 2008.

630 Bartsch, A., Gay, B. A., Schüttemeyer, D., et al.: Advancing the Arctic Methane Permafrost
631 Challenge (AMPAC) with future satellite missions, *IEEE J. Sel. Top. Appl. Earth Obs.*
632 *Remote Sens.*, 15, 1234–1245, <https://doi.org/10.1109/JSTARS.2025.3538897>, 2025.

633 Bogard, M. J., del Giorgio, P. A., Boutet, L., Chaves, M. C. G., Prairie, Y. T., Merante, A.,
634 and Derry, A. M.: Oxic water column methanogenesis as a major component of aquatic CH₄
635 fluxes, *Nat. Commun.*, 5, 5350, <https://doi.org/10.1038/ncomms6350>, 2014.

636 Bouranis, J. A., McGivern, B. B., Makke, G., et al.: Metabolic redox coupling controls
637 methane production in permafrost-affected peatlands through organic matter quality-
638 dependent energy allocation, *Glob. Change Biol.*, 31, e70390,
639 <https://doi.org/10.1111/gcb.70390>, 2025.

640 Bulínová, M., Schomacker, A., Kjellman, S. E., Gudasz, C., Olid, C., Rydberg, J., Panieri, G.,
641 et al.: Increased ecosystem productivity boosts methane production in Arctic lake sediments,
642 *J. Geophys. Res.-Biogeosci.*, 130, e2024JG008508, <https://doi.org/10.1029/2024JG008508>,
643 2025.

644 Emerson, J. B., Varner, R. K., Wik, M., Parks, D. H., Neumann, R. B., Johnson, J. E.,
645 Singleton, C. M., Woodcroft, B. J., Tollerson, R., Owusu-Domme, A., Binder, M., Freitas,
646 N. L., Crill, P. M., Saleska, S. R., Tyson, G. W., and Rich, V. I.: Diverse sediment microbiota
647 shape methane emission temperature sensitivity in Arctic lakes, *Nat. Commun.*, 12, 5815,
648 <https://doi.org/10.1038/s41467-021-25983-9>, 2021.

649 Callaghan, T. V., Christensen, T. R., and Jantze, E. J.: Plant and vegetation dynamics on
650 Disko island, west Greenland: Snapshots separated by over 40 years, *Ambio*, 40, 6,
651 <https://doi.org/10.1007/s13280-011-0169-x>, 2011.

652 Cheng, S., Meng, F., Wang, Y., Zhang, J., and Zhang, L.: The potential linkage between
653 sediment oxygen demand and microbes and its contribution to the dissolved oxygen depletion
654 in the Gan River, *Front. Microbiol.*, 15, 1413447,
655 <https://doi.org/10.3389/fmicb.2024.1413447>, 2024.

656 Christiansen, H. H.: Active layer monitoring in two Greenlandic permafrost areas:
657 Zackenberg and Disko Island, *Geogr. Tidsskr.*, 99, 1999.

658 Christiansen, J. R., Romero, A. J. B., Jørgensen, N. O. G., Glaring, M. A., Jørgensen, C. J.,
659 Berg, L. K., and Elberling, B.: Methane fluxes and the functional groups of methanotrophs
660 and methanogens in a young Arctic landscape on Disko Island, West Greenland,
661 *Biogeochemistry*, 122, <https://doi.org/10.1007/s10533-014-0026-7>, 2015.

662 Cole, J. J. and Caraco, N. F.: Atmospheric exchange of carbon dioxide in a low-wind
663 oligotrophic lake measured by the addition of SF6, *Limnol. Oceanogr.*, 43,
664 <https://doi.org/10.4319/lo.1998.43.4.0647>, 1998.

665 Conrad, R.: Microbial ecology of methanogens and methanotrophs, *Adv. Agron.*, 96,
666 [https://doi.org/10.1016/S0065-2113\(07\)96005-8](https://doi.org/10.1016/S0065-2113(07)96005-8), 2007.

667 Cunada, C. L., Lesack, L. F. W., Tank, S. E., and Hesslein, R. H.: Methane flux dynamics
668 among CO₂-absorbing and thermokarst lakes of a great Arctic delta, *Biogeochemistry*, 156,
669 25–39, <https://doi.org/10.1007/s10533-021-00853-0>, 2021.

670 D'Imperio, L., Nielsen, C. S., Westergaard-Nielsen, A., Michelsen, A., and Elberling, B.:
671 Methane oxidation in contrasting soil types: responses to experimental warming with
672 implication for landscape-integrated CH₄ budget, *Glob. Change Biol.*, 23,
673 <https://doi.org/10.1111/gcb.13400>, 2017.

674 Elder, C. D., Thompson, D. R., Thorpe, A. K., Hanke, P., Walter Anthony, K. M., and Miller,
675 C. E.: Airborne mapping reveals emergent power law of Arctic methane emissions, *Geophys.
676 Res. Lett.*, 47, <https://doi.org/10.1029/2019GL085707>, 2020.

677 Elith, J., Leathwick, J. R., and Hastie, T.: A working guide to boosted regression trees, *J.
678 Anim. Ecol.*, 77, <https://doi.org/10.1111/j.1365-2656.2008.01390.x>, 2008.

679 Emerson, J. B., Varner, R. K., Wik, M., Parks, D. H., Neumann, R. B., Johnson, J. E.,
680 Singleton, C. M., Woodcroft, B. J., Tollerson, R., Owusu-Dommey, A., Binder, M., Freitas,
681 N. L., Crill, P. M., Saleska, S. R., Tyson, G. W., and Rich, V. I.: Diverse sediment microbiota
682 shape methane emission temperature sensitivity in Arctic lakes, *Nat. Commun.*, 12,
683 <https://doi.org/10.1038/s41467-021-25983-9>, 2021.

684 Esposito, C., Nijman, T. P. A., Veraart, A. J., Audet, J., Levi, E. E., Lauridsen, T. L., and
685 Davidson, T. A.: Activity and abundance of methane-oxidizing bacteria on plants in
686 experimental lakes subjected to different nutrient and warming treatments, *Aquat. Bot.*, 185,
687 <https://doi.org/10.1016/j.aquabot.2022.103610>, 2023.

688 Fazi, S., Amalfitano, S., Venturi, S., Pacini, N., Vazquez, E., Olaka, L. A., Tassi, F.,
689 Crogna, S., Herzsprung, P., Lechtenfeld, O. J., Cabassi, J., Capecchiacci, F., Rossetti, S.,
690 Yakimov, M. M., Vaselli, O., Harper, D. M., and Butturini, A.: High concentrations of
691 dissolved biogenic methane associated with cyanobacterial blooms in East African lake
692 surface water, *Commun. Biol.*, 4, <https://doi.org/10.1038/s42003-021-02365-x>, 2021.

693 Fox-Kemper, B., Hewitt, H. T., Xiao, C., et al.: Chapter 9: Ocean, cryosphere and sea level
694 change, in: *Climate Change 2021: The Physical Science Basis. Contribution of Working
695 Group I to the Sixth Assessment Report of the Intergovernmental Panel on Climate Change*,
696 Cambridge University Press, 1211–1362, <https://doi.org/10.1017/9781009157896.011>, 2021.

697 Garcia, H. E. and Gordon, L. I.: Oxygen solubility in seawater: Better fitting equations,
698 *Limnol. Oceanogr.*, 37, <https://doi.org/10.4319/lo.1992.37.6.1307>, 1992.

699 Graef, C., Hestnes, A. G., Svenning, M. M., and Frenzel, P.: The active methanotrophic
700 community in a wetland from the High Arctic, *Environ. Microbiol. Rep.*, 3,
701 <https://doi.org/10.1111/j.1758-2229.2010.00237.x>, 2011.

702 Hall, R. O. and Madinger, H. L.: Use of argon to measure gas exchange in turbulent mountain
703 streams, *Biogeosciences*, 15, <https://doi.org/10.5194/bg-15-3085-2018>, 2018.

704 Heilman, M. A. and Carlton, R. G.: Methane oxidation associated with submersed vascular
705 macrophytes and its impact on plant diffusive methane flux, *Biogeochemistry*, 52, 207–224,
706 <https://doi.org/10.1023/A:1006427712846>, 2001.

707 Hijmans, R. J., Phillips, S., Leathwick, J., and Elith, J.: dismo: Species Distribution
708 Modeling, R package version 1.3-14 [code], <https://doi.org/10.32614/CRAN.package.dismo>,
709 2023.

710 Hoffmann, M., Schulz-Hanke, M., Garcia Alba, J., Jurisch, N., Hagemann, U., Sachs, T.,
711 Sommer, M., and Augustin, J.: A simple calculation algorithm to separate high-resolution
712 CH₄ flux measurements into ebullition- and diffusion-derived components, *Atmos. Meas.
713 Tech.*, 10, <https://doi.org/10.5194/amt-10-109-2017>, 2017.

714 Humlum, O.: Active layer thermal regime 1991–1996 at Qeqertarsuaq, Disko Island, Central
715 West Greenland, *Arct. Alp. Res.*, 30, <https://doi.org/10.2307/1551977>, 1998.

716 Humlum, O., Hansen, B. U., and Nielsen, N.: Meteorological observations 1998 at the arctic
717 station, Qeqertarsuaq (69°15'N), Central West Greenland, *Geogr. Tidsskr.*, 99,
718 <https://doi.org/10.1080/00167223.1999.10649428>, 1999.

719 Iannone, R. and Roy, O.: DiagrammeR: Graph/Network Visualization, R package version
720 1.0.11 [code], <https://doi.org/10.32614/CRAN.package.DiagrammeR>, 2024.

721 Juncher Jørgensen, C., Schlaikjær Mariager, T., and Riis Christiansen, J.: Spatial variation of
722 net methane uptake in Arctic and subarctic drylands of Canada and Greenland, *Geoderma*,
723 443, <https://doi.org/10.1016/j.geoderma.2024.116815>, 2024.

724 Klaus, M., Verheijen, H. A., Karlsson, J., and Seekell, D. A.: Depth and basin shape constrain
725 ecosystem metabolism in lakes dominated by benthic primary producers, *Limnol. Oceanogr.*,
726 67, 2763–2778, <https://doi.org/10.1002/lno.12236>, 2022.

727 Keskitalo, K. H., Bröder, L., Shakil, S., Zolkos, S., Tank, S. E., van Dongen, B. E., Tesi, T.,
728 Haghipour, N., Eglinton, T. I., Kokelj, S. V., and Vonk, J. E.: Downstream evolution of
729 particulate organic matter composition from permafrost thaw slumps, *Front. Earth Sci.*, 9,
730 <https://doi.org/10.3389/feart.2021.642675>, 2021.

731 Kleber, G. E., Magerl, L., Turchyn, A. V., Schloemer, S., Trimmer, M., Zhu, Y., and Hodson,
732 A.: Proglacial methane emissions driven by meltwater and groundwater flushing in a high-
733 Arctic glacial catchment, *Biogeosciences*, 22, 659–674, <https://doi.org/10.5194/bg-22-659-2025>, 2025.

735 Kluge, M., Wauthy, M., Clemmensen, K. E., Wurzbacher, C., Hawkes, J. A., Einarsdottir, K.,
736 Rautio, M., Stenlid, J., and Peura, S.: Declining fungal diversity in Arctic freshwaters along a
737 permafrost thaw gradient, *Glob. Change Biol.*, 27, <https://doi.org/10.1111/gcb.15852>, 2021.

738 Korrensalo, A., Alekseychik, P., Mammarella, I., et al.: High-resolution spatial patterns and
739 drivers of terrestrial ecosystem greenhouse gas fluxes in sub-Arctic Finland, *Biogeosciences*,
740 21, 335–352, <https://doi.org/10.5194/bg-21-335-2024>, 2024.

741 Kuhn, M. A., Varner, R. K., Bastviken, D., Crill, P., MacIntyre, S., Turetsky, M., Walter
742 Anthony, K., McGuire, A. D., and Olefeldt, D.: BAWLD-CH4: a comprehensive dataset of
743 methane fluxes from boreal and arctic ecosystems, *Earth Syst. Sci. Data*, 13, 5151–5189,
744 <https://doi.org/10.5194/essd-13-5151-2021>, 2021.

745 Kutzbach, L., Schneider, J., Sachs, T., Giebels, M., Nykänen, H., Shurpali, N. J.,
746 Martikainen, P. J., Alm, J., and Wilmking, M.: CO₂ flux determination by closed-chamber
747 methods can be seriously biased by inappropriate application of linear regression,
748 *Biogeosciences*, 4, 1005–2007, <https://doi.org/10.5194/bg-4-1005-2007>, 2007.

749 Kyzivat, E. D., Smith, L. C., Garcia-Tigreros, F., Huang, C., Wang, C., Langhorst, T., et al.:
750 The importance of lake emergent aquatic vegetation for estimating Arctic–Boreal methane
751 emissions, *J. Geophys. Res.-Biogeosci.*, 127, e2021JG006635,
752 <https://doi.org/10.1029/2021JG006635>, 2022.

753 Laanbroek, H. J.: Methane emission from natural wetlands: Interplay between emergent
754 macrophytes and soil microbial processes: A mini-review, *Ann. Bot.*, 105,
755 <https://doi.org/10.1093/aob/mcp201>, 2010.

756 Larsen, J. G. and Larsen, L. M.: Lithostratigraphy, geology and geochemistry of the Tertiary
757 volcanic rocks on Svartenhuk Halvø and adjoining areas, West Greenland, *GEUS Bull.*, 50,
758 <https://doi.org/10.34194/geusb.v50.8295>, 2022.

759 Liebner, S., Zeyer, J., Wagner, D., Schubert, C., Pfeiffer, E. M., and Knoblauch, C.: Methane
760 oxidation associated with submerged brown mosses reduces methane emissions from
761 Siberian polygonal tundra, *J. Ecol.*, 99, <https://doi.org/10.1111/j.1365-2745.2011.01823.x>,
762 2011.

763 Li, M., Peng, C., Zhu, Q., Zhou, X., Yang, G., Song, X., and Zhang, K.: The significant
764 contribution of lake depth in regulating global lake diffusive methane emissions, *Water Res.*,
765 172, 115465, <https://doi.org/10.1016/j.watres.2020.115465>, 2020.

766 Michel, G., Tonon, T., Scornet, D., Cock, J. M., and Kloareg, B.: Central and storage carbon
767 metabolism of the brown alga *Ectocarpus siliculosus*: Insights into the origin and evolution of
768 storage carbohydrates in eukaryotes, *New Phytol.*, 188, <https://doi.org/10.1111/j.1469-8137.2010.03345.x>, 2010.

770 Miner, K. R., Turetsky, M. R., Malina, E., Bartsch, A., Tamminen, J., McGuire, A. D., Fix,
771 A., Sweeney, C., Elder, C. D., and Miller, C. E.: Permafrost carbon emissions in a changing
772 Arctic, *Nat. Rev. Earth Environ.*, 3, <https://doi.org/10.1038/s43017-021-00230-3>, 2022.

773 Mulholland, P. J., Fellows, C. S., Tank, J. L., Grimm, N. B., Webster, J. R., Hamilton, S. K.,
774 Martí, E., Ashkenas, L., Bowden, W. B., Dodds, W. K., McDowell, W. H., Paul, M. J., and
775 Peterson, B. J.: Inter-biome comparison of factors controlling stream metabolism, *Freshw.
776 Biol.*, 46, <https://doi.org/10.1046/j.1365-2427.2001.00773.x>, 2001.

777 Myrstener, M., Sponseller, R. A., Bergström, A. K., and Giesler, R.: Organic carbon
778 availability regulates aquatic metabolism in a boreal stream network across land-use settings,
779 *Freshw. Biol.*, 66, 1899–1911, <https://doi.org/10.1111/fwb.13793>, 2021.

780 Neumann, R. B., Moorberg, C. J., Lundquist, J. D., Turner, J. C., Waldrop, M. P., McFarland,
781 J. W., Euskirchen, E. S., Edgar, C. W., and Turetsky, M. R.: Warming effects of spring
782 rainfall increase methane emissions from thawing permafrost, *Geophys. Res. Lett.*, 46,
783 <https://doi.org/10.1029/2018GL081274>, 2019.

784 Noss, C., Bodmer, P., Koca, K., and Lorke, A.: Flow and turbulence driven water surface
785 roughness and gas exchange velocity in streams, *E3S Web Conf.*, 40, 05018,
786 <https://doi.org/10.1051/e3sconf/20184005018>, 2018.

787 Olefeldt, D., Hovemyr, M., Kuhn, M. A., Bastviken, D., Bohn, T. J., Connolly, J., Crill, P.,
788 Euskirchen, E. S., Finkelstein, S. A., Genet, H., Grosse, G., Harris, L. I., Heffernan, L.,
789 Helbig, M., Hugelius, G., Hutchins, R., Juutinen, S., Lara, M. J., Malhotra, A., et al.: The
790 boreal-arctic wetland and lake dataset (BAWLD), *Earth Syst. Sci. Data*, 13,
791 <https://doi.org/10.5194/essd-13-5127-2021>, 2021.

792 Olid, C., Zannella, A., and Lau, D. C. P.: The role of methane transport from the active layer
793 in sustaining methane emissions and food chains in subarctic ponds, *J. Geophys. Res.-
794 Biogeosci.*, 126, <https://doi.org/10.1029/2020JG005810>, 2021.

795 Olid, C., Rodellas, V., Rocher-Ros, G., Garcia-Orellana, J., Diego-Feliu, M., Alorda-
796 Kleinglass, A., Bastviken, D., and Karlsson, J.: Groundwater discharge as a driver of methane
797 emissions from Arctic lakes, *Nat. Commun.*, 13, <https://doi.org/10.1038/s41467-022-31219-1>,
798 2022.

799 Pedersen, A. R., Petersen, S. O., and Schelde, K.: A comprehensive approach to soil-
800 atmosphere trace-gas flux estimation with static chambers, *Eur. J. Soil Sci.*, 61,
801 <https://doi.org/10.1111/j.1365-2389.2010.01291.x>, 2010.

802 QGIS Development Team: QGIS Geographic Information System, Open Source Geospatial
803 Foundation Project, <https://qgis.org>, n.d.

804 Rasilo, T., Prairie, Y. T., and del Giorgio, P. A.: Large-scale patterns in summer diffusive
805 CH₄ fluxes across boreal lakes, and contribution to diffusive carbon emissions, *Glob. Change
806 Biol.*, 21, 1124–1139, <https://doi.org/10.1111/gcb.12741>, 2015.

807 Rautio, M., Dufresne, F., Laurion, I., Bonilla, S., Vincent, W. F., and Christoffersen, K. S.:
808 Shallow freshwater ecosystems of the circumpolar Arctic, *Ecoscience*, 18,
809 <https://doi.org/10.2980/18-3-3463>, 2011.

810 Ravn, N. R., Elberling, B., and Michelsen, A.: Arctic soil carbon turnover controlled by
811 experimental snow addition, summer warming and shrub removal, *Soil Biol. Biochem.*, 142,
812 <https://doi.org/10.1016/j.soilbio.2019.107698>, 2020.

813 Rocher-Ros, G., Sponseller, R. A., Bergström, A.-K., Myrstener, M., and Giesler, R.: Stream
814 metabolism controls diel patterns and evasion of CO₂ in Arctic streams, *Glob. Change Biol.*,
815 26, 1400–1413, <https://doi.org/10.1111/gcb.14895>, 2020.

816 Saunois, M., Martinez, A., Poulter, B., Zhang, Z., Raymond, P. A., Regnier, P., Canadell, J.
817 G., Jackson, R. B., Patra, P. K., Bousquet, P., Ciais, P., Dlugokencky, E. J., Lan, X., Allen,
818 G. H., Bastviken, D., Beerling, D. J., Belikov, D. A., Blake, D. R., Castaldi, S., et al.: Global
819 methane budget 2000–2020, *Earth Syst. Sci. Data*, 17, 1873–1958,
820 <https://doi.org/10.5194/essd-17-1873-2025>, 2025.

821 Schuur, E. A. G., McGuire, A. D., Schädel, C., Grosse, G., Harden, J. W., Hayes, D. J.,
822 Hugelius, G., Koven, C. D., Kuhry, P., Lawrence, D. M., Natali, S. M., Olefeldt, D.,
823 Romanovsky, V. E., Schaefer, K., Turetsky, M. R., Treat, C. C., and Vonk, J. E.: Climate
824 change and the permafrost carbon feedback, *Nature*, 520,
825 <https://doi.org/10.1038/nature14338>, 2015.

826 Singleton, C. M., McCalley, C. K., Woodcroft, B. J., Boyd, J. A., Evans, P. N., Hodgkins, S.
827 B., Chanton, J. P., Frolking, S., Crill, P. M., Saleska, S. R., Rich, V. I., and Tyson, G. W.:
828 Methanotrophy across a natural permafrost thaw environment, *ISME J.*, 12,
829 <https://doi.org/10.1038/s41396-018-0065-5>, 2018.

830 Street, L. E., Dean, J. F., Billett, M. F., Baxter, R., Dinsmore, K. J., Lessels, J. S., Subke, J.
831 A., Tetzlaff, D., and Wookey, P. A.: Redox dynamics in the active layer of an Arctic
832 headwater catchment; examining the potential for transfer of dissolved methane from soils to
833 stream water, *J. Geophys. Res.-Biogeosci.*, 121, <https://doi.org/10.1002/2016JG003387>, 2016.

834 Stevenson, M. A., McGowan, S., Pearson, E. J., Swann, G. E. A., Leng, M. J., Jones, V. J.,
835 Bailey, J. J., Huang, X., and Whiteford, E.: Anthropocene climate warming enhances
836 autochthonous carbon cycling in an upland Arctic lake, Disko Island, West Greenland,
837 *Biogeosciences*, 18, <https://doi.org/10.5194/bg-18-2465-2021>, 2021.

838 Thompson, H. A., White, J. R., Pratt, L. M., and Sauer, P. E.: Spatial variation in flux, δ¹³C
839 and δ²H of methane in a small Arctic lake with fringing wetland in western Greenland,
840 *Biogeochemistry*, 131, 17–33, <https://doi.org/10.1007/s10533-016-0261-1>, 2016.

841 Vachon, D. and Prairie, Y. T.: The ecosystem size and shape dependence of gas transfer
842 velocity versus wind speed relationships in lakes, *Can. J. Fish. Aquat. Sci.*, 70, 1757–1764,
843 <https://doi.org/10.1139/cjfas-2013-0241>, 2013.

844 Virkkala, A. M., Niittynen, P., Kemppinen, J., Marushchak, M. E., Voigt, C., Hensgens, G.,
845 Kerttula, J., Happonen, K., Tyystjärvi, V., Biasi, C., Hultman, J., Rinne, J., and Luoto, M.:
846 High-resolution spatial patterns and drivers of terrestrial ecosystem carbon dioxide, methane,
847 and nitrous oxide fluxes in the tundra, *Biogeosciences*, 21, <https://doi.org/10.5194/bg-21-335-2024>, 2024.

849 Walter Anthony, K. M., Anthony, P., Grosse, G., and Chanton, J.: Geologic methane seeps
850 along boundaries of Arctic permafrost thaw and melting glaciers, *Nat. Geosci.*, 5,
851 <https://doi.org/10.1038/ngeo1480>, 2012.

852 Walter Anthony, K., Schneider von Deimling, T., Nitze, I., Frolking, S., Emond, A., Daanen,
853 R., Anthony, P., Lindgren, P., Jones, B., and Grosse, G.: 21st-century modeled permafrost
854 carbon emissions accelerated by abrupt thaw beneath lakes, *Nat. Commun.*, 9,
855 <https://doi.org/10.1038/s41467-018-05738-9>, 2018.

856 Walvoord, M. A. and Kurylyk, B. L.: Hydrologic impacts of thawing permafrost—A review,
857 *Vadose Zone J.*, 15, <https://doi.org/10.2136/vzj2016.01.0010>, 2016.

858 Wallenius, A. J., Dalcin Martins, P., Slomp, C. P., and Jetten, M. S. M.: Anthropogenic and
859 environmental constraints on the microbial methane cycle in coastal sediments, *Front. Microbiol.*, 12, <https://doi.org/10.3389/fmicb.2021.631621>, 2021.

861 Westergaard-Nielsen, A., Balstrøm, T., Treier, U. A., Normand, S., and Elberling, B.:
862 Estimating meltwater retention and associated nitrate redistribution during snowmelt in an
863 Arctic tundra landscape, *Environ. Res. Lett.*, 15, <https://doi.org/10.1088/1748-9326/ab57b1>,
864 2020.

865 Winslow, L. A., Zwart, J. A., Batt, R. D., Dugan, H. A., Woolway, R. I., Corman, J. R.,
866 Hanson, P. C., and Read, J. S.: LakeMetabolizer: an R package for estimating lake
867 metabolism from free-water oxygen using diverse statistical models, *Inland Waters*, 6,
868 <https://doi.org/10.1080/IW-6.4.883>, 2016.

869 Wickham, H.: *ggplot2: Elegant Graphics for Data Analysis*, Springer-Verlag, New York,
870 <https://doi.org/10.1007/978-3-319-24277-4>, 2016.

871 Xu, W., Lambæk, A., Holm, S. S., Furbo-Halken, A., Elberling, B., and Ambus, P. L.: Effects
872 of experimental fire in combination with climate warming on greenhouse gas fluxes in Arctic
873 tundra soils, *Sci. Total Environ.*, 795, <https://doi.org/10.1016/j.scitotenv.2021.148847>, 2021.

874 Yuan, K., Li, F., McNicol, G., Chen, M., Hoyt, A., Knox, S., Riley, W. J., Jackson, R., and
875 Zhu, Q.: Boreal–Arctic wetland methane emissions modulated by warming and vegetation
876 activity, *Nat. Clim. Change*, 14, <https://doi.org/10.1038/s41558-024-01933-3>, 2024.

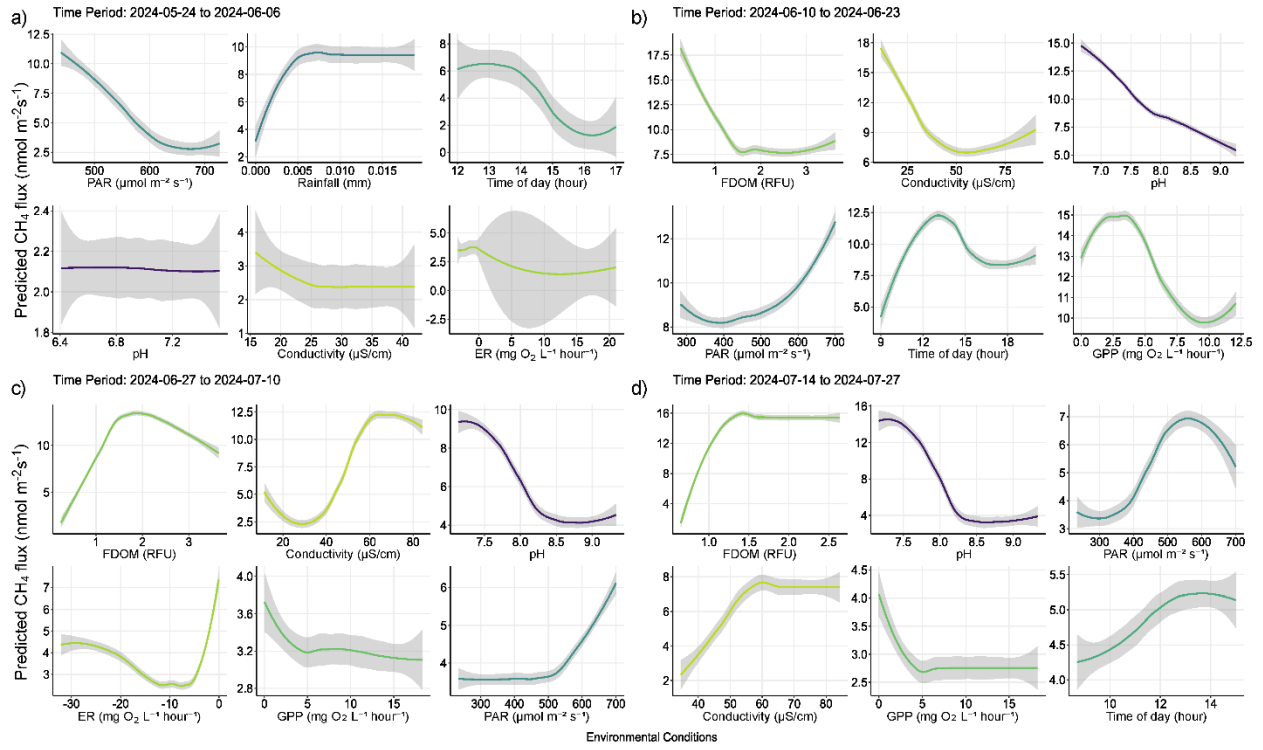
877 Žárský, J. D., Kohler, T. J., Yde, J. C., Falteisek, L., Lamarche-Gagnon, G., Hawkings, J. R.,
878 Hatton, J. E., and Stibal, M.: Prokaryotic assemblages in suspended and subglacial sediments

879 within a glacierized catchment on Qeqertarsuaq (Disko Island), west Greenland, *FEMS*
880 *Microbiol. Ecol.*, 94, <https://doi.org/10.1093/femsec/fiy100>, 2018.

881 Zastruzny, S. F., Elberling, B., Nielsen, L., and Jensen, K. H.: Water flow in the active layer
882 along an arctic slope—An investigation based on a field campaign and model simulations,
883 *egusphere* [preprint], *The Cryosphere Discuss.*, 1–32, <https://doi.org/10.5194/tc-2017-97>,
884 2017.

885

886 **Appendix A**



887

888 Figure A1. Partial dependency plots illustrating predicted marginal effects of meteorological, and
 889 biochemical water conditions predicting diffusive CH_4 fluxes. Each figure represents the direct
 890 marginal effect on CH_4 fluxes when all other predictors are held at their median, therefore giving a
 891 more mechanistic understanding of those conditions and processes regulating fluxes from water
 892 surfaces. The figures are ordered by importance in each time period and colors correspond to those
 893 seen in Figure 6 of the main text. The colored lines represent the result of a fitted general additive
 894 model ($y \sim s(x)$) and thus a smooth representation across the 321 fitted BRT models. Each predictor
 895 and its numerical range are given on the x-axis, while predicted fluxes are given on the y-axis.

896



906 Figure A2. Image showing the various microbial forms encountered and found to influence CH₄
907 fluxes from the catchment area. In the photo on the far left we can see gas film on the water surface
908 which was associated with submerged iron-oxidizing microbial assemblages, i.e. similar to what is
909 shown in the middle photo, however exposed to the atmosphere in lower water levels. The photo on
910 the right shows a brown alga which formed in the warm spring area southeast of the lake. In all
911 cases, increased fluxes were generally encountered when measuring atop the middle and right
912 microbial assemblages.

913